

# The mixing of $D_{s1}(2460)$ and $D_{s1}(2536)$

Xiao-Gang Wu<sup>1\*</sup> and Qiang Zhao<sup>1,2†</sup>

1) *Institute of High Energy Physics, Chinese Academy of Sciences, Beijing 100049, P.R. China* and

2) *Theoretical Physics Center for Science Facilities, CAS, Beijing 100049, P.R. China*

(Dated: February 25, 2024)

The mixing mechanism of axial-vectors  $D_{s1}(2460)$  and  $D_{s1}(2536)$  is studied via intermediate hadron loops, e.g.  $D^*K$ , to which both states have strong couplings. By constructing the two-state mixing propagator matrix that respects the unitarity constraint and calculating the vertex coupling form factors in a chiral quark model, we can extract the masses, widths and mixing angles of the physical states. Two poles can be identified in the propagator matrix. One is at  $\sqrt{s} = 2454.5$  MeV corresponding to  $D_{s1}(2460)$  and the other at  $\sqrt{s} = (2544.9 - 1.0i)$  MeV corresponding to  $D_{s1}(2536)$ . For  $D_{s1}(2460)$ , a large mixing angle  $\theta = 47.5^\circ$  between  $^3P_1$  and  $^1P_1$  is obtained. It is driven by the real part of the mixing matrix element and corresponds to  $\theta' = 12.3^\circ$  between the  $j = 1/2$  and  $j = 3/2$  state mixing in the heavy quark limit. For  $D_{s1}(2536)$ , a mixing angle  $\theta = 39.7^\circ$  which corresponds to  $\theta' = 4.4^\circ$  in the heavy quark limit is found. An additional phase angle  $\phi = -6.9^\circ \sim 6.9^\circ$  is needed at the pole mass of  $D_{s1}(2536)$  since the mixing matrix elements are complex numbers. Both the real and imaginary part are found important for the large mixing angle. We show that the new experimental data from BaBar provide a strong constraint on the mixing angle at the mass of  $D_{s1}(2536)$ , from which two values can be extracted, i.e.  $\theta_1 = 32.1^\circ$  or  $\theta_2 = 38.4^\circ$ . Our study agrees well with the latter one. Detailed analysis of the mass shift procedure due to the coupled channel effects is also presented.

PACS numbers: 13.25.Ft, 14.40.Lb

## I. INTRODUCTION

In the past few years one of the most important experimental progresses in the study of the charmed meson spectrum is the establishment of the lowest  $P$ -wave charmed-strange mesons, i.e.  $D_{s0}(2317)$ ,  $D_{s1}(2460)$ ,  $D_{s1}(2536)$ , and  $D_{s2}(2573)$  as now listed in Particle Data Group (PDG) 2010 Edition [1]. Since the first observation by BaBar Collaboration [2], the spin-0 state  $D_{s0}(2317)$  and spin-1  $D_{s1}(2460)$  (later confirmed by Belle [3] and CLEO [4]) have initiated tremendous interests in its property and internal structure. These two states have masses lower than the potential model predictions, and their widths are rather narrow. It is somehow agreed that their low masses are caused by the open  $DK$  and  $D^*K$  thresholds, respectively, and as a consequence, their narrow decay widths are due to the dominant isospin-violating decays, i.e.  $D_{s0}(2317) \rightarrow D_s\pi$  and  $D_{s1}(2460) \rightarrow D_s^*\pi$  (see the review of Refs. [5, 6] and references therein).

The heavy-light  $Q\bar{q}$  system is an ideal platform for testing the internal constituent quark degrees of freedom. In the heavy quark limit the heavy quark spin is conserved and decoupled from the light quark degrees of freedom, which are characterized by the total angular momentum  $\mathbf{j}_q \equiv \mathbf{s}_q + \mathbf{L}$ , where  $\mathbf{s}_q$  is the light quark spin and  $\mathbf{L}$  is its orbital angular momentum. With  $j_q = 1/2$  and  $j_q = 3/2$ , one can arrange those four  $P$ -wave states into two classes, i.e.  $J^P = 0^+, 1^+$  and  $J^P = 1^+, 2^+$ , respectively, where  $J$  is the meson spin as a sum of the heavy quark spin  $\mathbf{S}_Q$  and  $\mathbf{j}_q$ . For the axial vector states in the charmed and charmed-strange meson spectrum, since they are not charge conjugation eigenstates, state mixings between the  $^3P_1$  and  $^1P_1$  configurations are allowed. In the case of charmed and charmed-strange heavy-light system when the heavy quark symmetry is broken at order of  $1/m_c$ , it would be interesting to study the mechanism that causes deviations from the ideal mixing scenario, i.e. breakdown of the heavy quark symmetry. This forms our motivation in this work. As mentioned earlier,  $D_{s1}(2460)$  and  $D_{s1}(2536)$  lie near the threshold of  $D^*K$  and both couple to  $D^*K$  strongly via a relative  $S$  wave. It gives rise to coupled channel effects in the mass shifts of potential quark model calculations in comparison with the observed values [7–9], and produces state mixings between the  $^3P_1$  and  $^1P_1$  configurations. Similar mechanism has been studied in the  $a_0(980)$ - $f_0(980)$  mixing in Ref. [10]. Determination of the mixing angle should be useful for understanding the property and internal structure of these two axial vector states.

---

\*Electronic address: wuxiaogang@ihep.ac.cn

†Electronic address: zhaoq@ihep.ac.cn

We mention that various solutions have been proposed in the literature to explain the observed results for  $D_{s1}(2460)$  and  $D_{s1}(2536)$ . For instance,  $D^*K$  molecule or tetra-quark configuration have been investigated in Refs. [11–13]. In Ref. [14],  $D_{s1}(2460)$  is explained as a dynamically generated state. The mixing angle has also been calculated in the quark model [15, 16] but with large uncertainties from the quark spin-orbital interactions. In this work, we investigate the two-state mixing propagator matrix which respects the unitarity constraint in a chiral quark model. We will show that the coupled channel effects via intermediate hadron loops can provide a simultaneous determination of the masses, widths and mixing angles of these two axial vector states. We also mention that the coupled channel effects on the  $^3P_1$  and  $^1P_1$  mixing was recently studied in Ref. [17], where the the couplings were extracted in the  $^3P_0$  model and a subtracted dispersion relation was applied to evaluate the hadron loops. In our approach we use the chiral quark model to extract the couplings and vertex form factor. We then extend the quark model form factor to a covariant form which can be applied on a general ground to much broader cases.

The paper is organized as follows. In Sec. II, we give the basic formulas of two-state mixings via coupled channel propagators. In Sec. III, the relevant coupling form factors are determined by the chiral quark model. In Sec. IV the propagator matrix is calculated in detail. Section V is devoted to show our numerical results for the mass and mixing parameters. The experimental constraints for the mixing angle are presented in Sec. VI. A summary is given in the last Section. In Appendix A the detailed definition and calculation of a special function used in the evaluation of the loop integrals with exponential form factors are provided.

## II. MIXING THROUGH COUPLED CHANNEL EFFECT

We use  $|a\rangle$  and  $|b\rangle$  to present two pure states in the quark model. If they can couple to common final states, there will be a transition between them via single particle irreducible (1PI) diagrams as shown in Fig. 1.

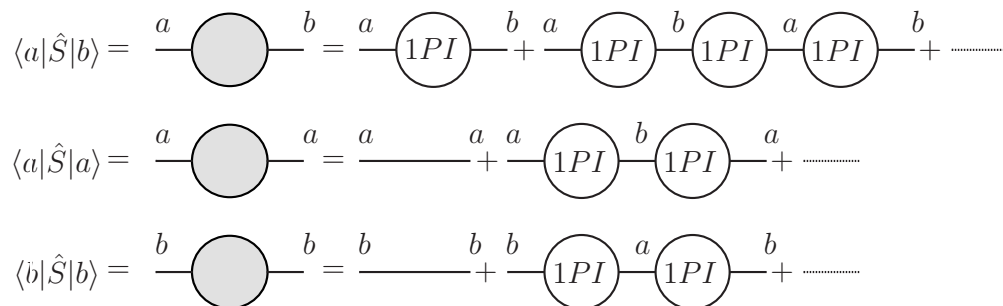


FIG. 1: Transition through intermediate states

The propagator matrix of  $|a\rangle$  and  $|b\rangle$  can be expressed as

$$G_{ab} = \begin{pmatrix} \langle a| \\ \langle b| \end{pmatrix} \hat{S} (|a\rangle, |b\rangle) . \quad (1)$$

The physical states  $|A\rangle$  and  $|B\rangle$  should be a mixture of  $|a\rangle$  and  $|b\rangle$ ,

$$\begin{pmatrix} |A\rangle \\ |B\rangle \end{pmatrix} = \begin{pmatrix} \cos\theta & -\sin\theta e^{i\phi} \\ \sin\theta e^{-i\phi} & \cos\theta \end{pmatrix} \begin{pmatrix} |a\rangle \\ |b\rangle \end{pmatrix} = R(\theta, \phi) \begin{pmatrix} |a\rangle \\ |b\rangle \end{pmatrix} \quad (2)$$

where  $R(\theta, \phi)$  is the mixing matrix,  $\theta$  is the mixing angle, and  $\phi$  is a possible relative phase between  $|a\rangle$  and  $|b\rangle$ . Then the propagator matrix of  $|A\rangle$  and  $|B\rangle$  is

$$G_{AB} = R G_{ab} R^\dagger . \quad (3)$$

The physical propagator matrix  $G_{AB}$  should be a diagonal matrix. Thus, we can determine the mixing parameters  $\{\theta, \phi\}$  by diagonalizing the propagator matrix  $G_{ab}$ .

In the present case, we set  $|a\rangle = |^3P_1\rangle$ ,  $|b\rangle = |^1P_1\rangle$ ,  $|A\rangle = |D_{s1}(2460)\rangle$  and  $|B\rangle = |D_{s1}(2536)\rangle$  as in Ref. [8]. The mixing scheme is

$$\begin{aligned} |D_{s1}(2460)\rangle &= \cos\theta|^3P_1\rangle - \sin\theta e^{i\phi}|^1P_1\rangle \\ |D_{s1}(2536)\rangle &= \sin\theta e^{-i\phi}|^3P_1\rangle + \cos\theta|^1P_1\rangle, \end{aligned} \quad (4)$$

where states  $|^3P_1\rangle$  and  $|^1P_1\rangle$  can be rotated to the eigenstates in the heavy quark limit:

$$\begin{pmatrix} |^3P_1\rangle \\ |^1P_1\rangle \end{pmatrix} = \begin{pmatrix} \sqrt{\frac{2}{3}} & \sqrt{\frac{1}{3}} \\ -\sqrt{\frac{1}{3}} & \sqrt{\frac{2}{3}} \end{pmatrix} \begin{pmatrix} |j = \frac{1}{2}\rangle \\ |j = \frac{3}{2}\rangle \end{pmatrix}. \quad (5)$$

The mixing angle  $\theta$  defined in Eq. (4) can be related to  $\theta'$  defined in  $j = 1/2$  and  $j = 3/2$  bases:

$$\theta = \theta' + 35.26^\circ. \quad (6)$$

Considering parity conservation, the important intermediate states that can couple to  $D_{s1}(2460)$  and  $D_{s1}(2536)$  are  $D^*K$ ,  $D_s^*\eta$  and  $DK^*$ , of which the thresholds are listed in Table I.

TABLE I: The thresholds of intermediate states for  $D_{s1}(2460)$  and  $D_{s1}(2536)$ .

Intermediate states	$D^{*0}K^+$	$D^{*+}K^0$	$D_s^*\eta$	$D^0K^{*+}$	$D^+K^{*0}$
Threshold (GeV)	2.501	2.508	2.660	2.756	2.761

If all the particles involved are scalars or pseudoscalars, Fig. 1 will only represent sums of infinite geometric series and the resulting propagator matrix  $G$  becomes [10]

$$G_{ab} = \frac{1}{D_a D_b - D_{ab}^2} \begin{pmatrix} D_b & D_{ab} \\ D_{ba} & D_a \end{pmatrix}, \quad (7)$$

where  $D_a$  and  $D_b$  are the denominators of the single propagators of  $|a\rangle$  and  $|b\rangle$ , respectively, and the mixing term  $D_{ab}$  is the sum of all 1PI diagrams, which satisfies  $D_{ba} = D_{ab}$ . But from Table I, we find that the particles involved in the present case can be scalars, vectors or axial-vectors. There are five diagrams for the mixing of  $D_{s1}(2460)$  and  $D_{s1}(2536)$  as shown in Fig. 2.

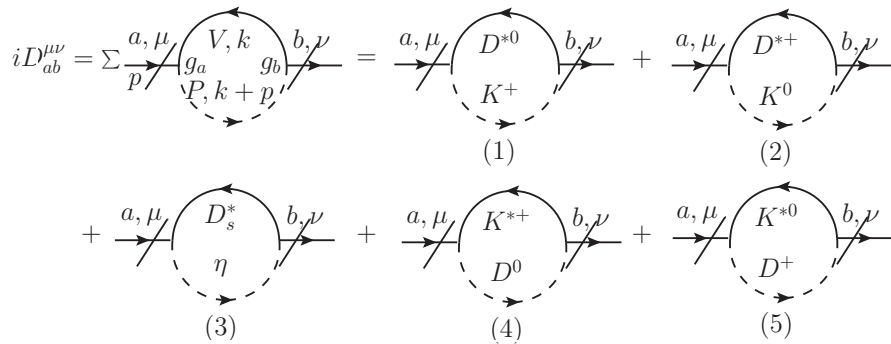


FIG. 2: Mixing term for  $D_{s1}(2460)$  and  $D_{s1}(2536)$ .

The mixing term can be generally divided into transverse and longitudinal terms:

$$D_{ab}^{\mu\nu} \equiv \Pi_{ab} P^{\mu\nu} + B_{ab} Q^{\mu\nu}, \quad (8)$$

where  $P^{\mu\nu} \equiv g^{\mu\nu} - p^\mu p^\nu / p^2$  and  $Q^{\mu\nu} \equiv p^\mu p^\nu / p^2$  are the transverse and longitudinal projector, respectively, and satisfy

$$P^{\mu\nu} P_\nu^\lambda = P^{\mu\lambda}, \quad Q^{\mu\nu} Q_\nu^\lambda = Q^{\mu\lambda}, \quad P^{\mu\nu} Q_\nu^\lambda = 0. \quad (9)$$

Next we concentrate on the evaluation of the propagator matrix  $G^{\mu\nu}$  for axial vector states. The numerator of the vector propagator is  $g^{\mu\nu} - p^\mu p^\nu / m^2$  and can be generally expressed as  $P^{\mu\nu} + \Delta Q^{\mu\nu}$  where  $\Delta = 1 - p^2 / m^2$ . With the properties of Eq.(9), the geometric sums, e.g.  $\langle a | \hat{S} | b \rangle$  in Fig. 1, can be taken for the transverse and longitudinal terms independently. After include the self-energy functions  $\Pi_a^{\mu\nu}$  and  $\Pi_b^{\mu\nu}$ , the complete propagator matrix for the  $1^3P_1$  and  $1^1P_1$  states becomes

$$G_{ab}^{\mu\nu} = iP^{\mu\nu} \frac{\bar{G}_{ab}(s)}{\det \bar{G}_{ab}(s)} + iQ^{\mu\nu} \frac{G_{ab}^L}{\det G_{ab}^L}, \quad (10)$$

with

$$\bar{G}_{ab}(s) \equiv M_{ab}^2 - \delta_{ab}s = \begin{pmatrix} m_b^2 + \Pi_b(s) - s & -\Pi_{ab}(s) \\ -\Pi_{ab}(s) & m_a^2 + \Pi_a(s) - s \end{pmatrix}, \quad (11)$$

and

$$G_{ab}^L(s) = \begin{pmatrix} \frac{m_b^2 - s}{\Delta_b} + B_b(s) & -B_{ab}(s) \\ -B_{ab}(s) & \frac{m_a^2 - s}{\Delta_a} + B_a(s) \end{pmatrix}, \quad (12)$$

where  $M_{ab}^2$  is the mass matrix. After diagonalization, the mass matrix becomes

$$M_{AB}^2 = R M_{ab}^2 R^\dagger = \begin{pmatrix} m_B^2 & 0 \\ 0 & m_A^2 \end{pmatrix}. \quad (13)$$

Note that the longitudinal term  $G_{ab}^L / \det G_{ab}^L$  is nonvanishing, but the poles are only related to the transverse term  $\bar{G}_{ab}$ .

By searching for the poles in the propagator matrix  $G^{\mu\nu}(s)$ , which is equivalent to set  $\det \bar{G}(s) = 0$ , we can obtain the masses and widths of the physical states. In general, there are two solutions  $s_A$  and  $s_B$  for the two state system. We can also extract the mixing angle  $\theta_{A,B}$  and the relative phase angle  $\phi_{A,B}$ . These mixing parameters are different for these two states, since they are extracted at the physical masses of these two states, respectively. If  $G$  is a normal matrix, which means  $GG^\dagger = G^\dagger G$ , then it can be diagonalized through a unitary transformation  $R$ . The resulting mixing angle  $\theta$  and relative phase  $\phi$  can thus be uniquely determined. Otherwise, we can only get a quasi-diagonalized matrix through the unitary transformation  $R$ . The reason is because that orthogonality cannot be satisfied between these two physical states.

### III. COUPLING FORM FACTORS IN THE CHIRAL QUARK MODEL

At hadronic level all the vertices in Fig. 2 involve the Axial-Vector-Pseudoscalar (AVP) type of coupling. In general, the AVP coupling vertex contains two coupling constants  $g_S$  and  $g_D$  representing the  $S$  and  $D$  waves as shown in Fig. 3.

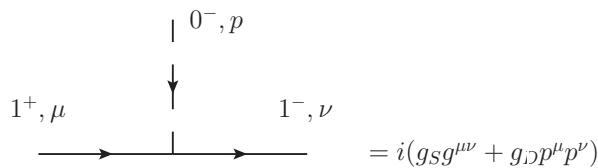


FIG. 3: The AVP vertex via the  $S$  and  $D$  wave couplings.

Since the decay momentum is small near the threshold, we expect that contributions from the  $D$ -wave coupling would be small. As a reasonable approximation, we omit  $g_D$  and keep  $g_S$  to the order  $O(v^0)$ . In the multipole approach, the helicity amplitude for  $1^+ \rightarrow 1^- + 0^-$  takes the form [18]

$$A_\nu = \langle S_f, \nu; 0, 0 | \hat{S} | S_i, \nu \rangle = \sum_L \langle L, 0; S_f, \mu | S_i, \nu \rangle Y_{L0}(\hat{q}) G_L, \quad (14)$$

where  $G_L$  is the coupling constant for the  $L$  wave and  $\hat{q}$  is the momentum direction of the final state particle in the center of mass frame of the initial state. In the present case, Eq. (14) becomes

$$\begin{bmatrix} A_0 \\ A_1 \end{bmatrix} = \begin{bmatrix} \frac{1}{2\sqrt{\pi}} & -\frac{1}{\sqrt{2\pi}} \\ \frac{1}{2\sqrt{\pi}} & \frac{1}{2\sqrt{2\pi}} \end{bmatrix} \begin{bmatrix} G_S \\ G_D \end{bmatrix}. \quad (15)$$

In order to obtain  $g_S$  to the order  $O(v^0)$ , we set

$$g_S = A_0(\vec{q} \rightarrow 0) = A_1(\vec{q} \rightarrow 0). \quad (16)$$

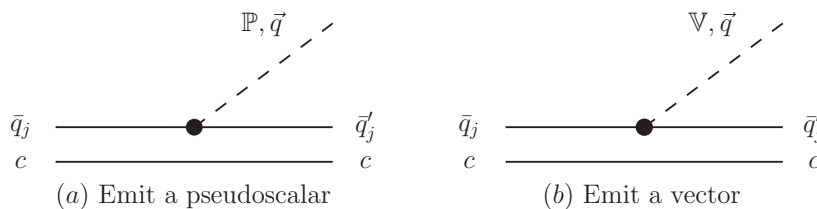


FIG. 4: Pseudoscalar (a) and vector meson (b) emission via an active light quark  $j$  in an effective chiral quark model.

### A. Coupling to $D^*K$ and $D_s^*\eta$

One notices that at all the coupling vertices the interacting quarks involve only light quark, i.e.  $u$ ,  $d$  and  $s$ . By treating the light mesons, pseudoscalar and vector mesons, as induced fields by a chiral Lagrangian for the mesons coupling to constituent quarks [19], the light and heavy quark degrees of freedom can be separated out in terms of nonrelativistic expansions near the decay threshold. This approach has been successfully applied to light meson productions in photo-nucleon and meson-nucleon scatterings [20–26] and strong decays of heavy-light mesons [27, 28] recently.

In the chiral quark model, we treat the pseudoscalar mesons  $K$  and  $\eta$  as the effective chiral fields as shown in Fig. 4(a). For emitting a pseudoscalar from an active quark line, the quark-meson coupling and corresponding non-relativistic form are respectively as follows [27]:

$$H_m = \sum_j \frac{1}{f_m} \hat{I}_j \bar{\psi}_j \gamma_\mu^j \gamma_5^j \psi_j \partial^\mu \phi_m, \quad (17)$$

$$H_m^{nr} = \sum_j \frac{1}{f_m} \left\{ G \boldsymbol{\sigma}_j \cdot \mathbf{q} + h \boldsymbol{\sigma}_j \cdot \mathbf{p}_j' \right\} \hat{I}_j \exp(-i\mathbf{q} \cdot \mathbf{r}_j), \quad (18)$$

with

$$G \equiv - \left( 1 + \frac{\omega}{E_f + M_f} \right), \quad h \equiv \frac{\omega}{2\mu_q}, \quad (19)$$

where  $f_m$  is the decay constant of the pseudoscalar meson,  $\hat{I}_j$  the isospin operator,  $\omega$  the energy of the pseudoscalar,  $M_f$  and  $E_f$  the mass and energy of the final state heavy meson,  $\mu_q$  a reduced mass given by  $1/\mu_q \equiv 1/m_j + 1/m'_j$ ,  $\mathbf{p}_j^{i'}$  and  $\mathbf{r}_j$  the internal momentum and coordinate for the light ( $j$ th) quark of the final state heavy meson.

Following the procedure in [27], we derive the helicity amplitude  $A_\nu^q \equiv \langle S_f, \nu | \hat{H}_m | S_i, \nu \rangle$  in the quark level. For  $1^3P_1 \rightarrow 1^3S_1 + \mathbb{P}$ , the explicit expressions are

$$A_0^q = ig_1 h \alpha \exp(-\frac{q_1^2}{4\alpha^2}), \quad A_1^q = i \frac{g_1}{4\alpha} [2Gqq_1 + h(4\alpha^2 - q_1^2)] \exp(-\frac{q_1^2}{4\alpha^2}), \quad (20)$$

and for  $1^1P_1 \rightarrow 1^3S_1 + \mathbb{P}$ , we have

$$A_0^q = -i \frac{g_1}{2\sqrt{2}\alpha} [2Gqq_1 + h(2\alpha^2 - q_1^2)] \exp(-\frac{q_1^2}{4\alpha^2}), \quad A_1^q = -\frac{i}{\sqrt{2}} g_1 h \alpha \exp(-\frac{q_1^2}{4\alpha^2}), \quad (21)$$

where  $g_1 = \langle \mathbb{M}_f | \hat{I}_1 | \mathbb{M}_i \rangle$  is the isospin factor,  $\alpha$  the harmonic oscillator strength  $\alpha \equiv \beta (2m_2/(m_1 + m_2))^{1/4}$  as in Ref. [27], and  $q_1 \equiv qm_2/(m_1 + m_2)$ . In the  $c\bar{s}$  system, the 1st quark is  $\bar{s}$  and the 2nd is  $c$  quark, and the flavor symmetry between the heavy and light quark is apparently broken.

By taking equivalence between the quark and hadron level helicity amplitudes, we can extract the coupling form factor as follows:

$$A_\nu = \sqrt{(E_i + M_i)(E_f + M_f)} A_\nu^q. \quad (22)$$

Then from Eqs.(16), (20) and (21), we finally obtain:

$$\text{for } 1^3P_1, \quad g_S = -\frac{\delta}{f_m} \sqrt{2M_i(E_f + M_f)} \cdot g_1 h \alpha \exp(-\frac{q_1^2}{4\alpha^2}), \quad (23)$$

$$\text{for } 1^1P_1, \quad g_S = \frac{\delta}{f_m} \sqrt{2M_i(E_f + M_f)} \cdot \frac{1}{\sqrt{2}} g_1 h \alpha \exp(-\frac{q_1^2}{4\alpha^2}), \quad (24)$$

where  $\delta$  is a global parameter accounts for the strength of the quark-meson couplings as introduced in [27].

## B. Coupling to $DK^*$

In this coupling, the vector meson  $K^*$  is treated as an effective chiral field, for which the effective quark-vector-meson coupling Lagrangian and the corresponding non-relativistic coupling form [22, 29] are

$$\hat{H}_v = \sum_j a \bar{\psi}_j \gamma_\mu^j \phi_\nu^\mu \psi_j, \quad (25)$$

$$\hat{H}_v^T = \sum_j \left\{ -\frac{\mathbf{p}_j^{i'} \cdot \boldsymbol{\epsilon}^*}{2\mu_q} + i\boldsymbol{\sigma}_j \cdot \mathbf{q} \times \boldsymbol{\epsilon}^* \left( \frac{1}{2m_j} + \frac{1}{E_f + M_f} - \frac{m'_j}{2M'm_j} \right) \right\} a \hat{I}_j \exp(-i\mathbf{q} \cdot \mathbf{r}_j), \quad (26)$$

$$\hat{H}_v^L = \sum_j \left\{ \left[ \frac{q}{\mu} \left( 1 - \frac{\omega}{2m_j} \right) + \frac{q\omega}{2M'\mu} + \frac{q\omega m'_j}{2M'\mu m_j} \right] - \frac{\omega}{2\mu\mu_q} \mathbf{p}_j^{i'} \cdot \hat{\mathbf{q}} \right\} a \hat{I}_j \exp(-i\mathbf{q} \cdot \mathbf{r}_j), \quad (27)$$

where  $\mu$ ,  $\omega$  and  $\boldsymbol{\epsilon}$  are the mass, energy and polarization vector of the emitted vector meson,  $M'$  the sum of the constituent quark mass of the final meson,  $a$  the overall quark-vector-meson coupling, and other symbols have the same meaning as those in Eqs.(17)-(19). Using the above operators, we can extract the helicity amplitudes  $A_\nu^q$ , i.e. for  $1^3P_1 \rightarrow 1^1S_0 + \mathbb{V}$ ,

$$A_1^q = -\frac{i}{2\sqrt{2}} a g_1 B \frac{q_1}{\alpha} \exp(-\frac{q_1^2}{4\alpha^2}), \quad A_0^q = 0, \quad (28)$$

and for  $1^1P_1 \rightarrow 1^1S_0 + \mathbb{V}$ ,

$$A_1^q = i a g_1 A \alpha \exp(-\frac{q_1^2}{4\alpha^2}), \quad A_0^q = \frac{i}{\sqrt{2}} a g_1 \left[ -C \frac{q_1}{\alpha} + D \alpha \left( \frac{q_1^2}{2\alpha^2} - 1 \right) \right] \quad (29)$$

with

$$A \equiv -\frac{1}{2\sqrt{2}\mu_q}, \quad (30)$$

$$B \equiv -\sqrt{2}q \left( \frac{1}{2m_j} + \frac{1}{E_f + M_f} - \frac{m'_j}{2M'm_j} \right), \quad (31)$$

$$C \equiv -\left[ \frac{q}{\mu} \left( 1 - \frac{\omega}{2m_j} \right) + \frac{q\omega}{2M'\mu} + \frac{q\omega m'_j}{2M'\mu m_j} \right], \quad (32)$$

$$D \equiv \frac{\omega}{2\mu\mu_q}. \quad (33)$$

Substituting Eqs. (28) and (29) to Eqs. (16) and (22), we obtain

$$\text{for } 1^3P_1, \quad g_S = 0, \quad (34)$$

$$\text{for } 1^1P_1, \quad g_S = -\sqrt{(E_i + M_i)(E_f + m_f)} \cdot \frac{1}{\sqrt{2}} ag_1 \frac{\alpha}{\mu_q} \exp\left(-\frac{q_1^2}{4\alpha^2}\right). \quad (35)$$

The coupling  $g_S = 0$  in Eq. (34) is because  $A_1^q$  in Eqs. (28) is proportional to  $q_1$ . Thus, the effective coupling vanishes below the open decay threshold. As a consequence, the contributions from Fig. 2(4) and (5) should vanish to the order  $O(v^0)$ . Therefore, we only need to consider the contributions from Fig. 2(1-3) in the following calculations.

### C. Numerical results for couplings

In the numerical calculation, we set  $|\vec{q}| = 0$  when the initial state lies below the threshold for  $\mathbb{VP}$  final state [29]. We adopt  $\eta = \frac{1}{\sqrt{3}}(u\bar{u} + d\bar{d} - s\bar{s})$  in the  $\eta - \eta'$  mixing scheme which corresponds to  $\theta_P = -\arcsin(1/3) = -19.47^\circ$  for the flavor octet and singlet mixing. Since the contribution from the  $D_s^*\eta$  loop is small, the uncertainties with  $\theta_P$  have only negligible effects on the mixing matrix. We obtain isospin factors  $g_1$  for different intermediate states as listed in Table II.

TABLE II: Isospin factors  $g_1$  extracted in the quark model.

$1^3P_1/1^1P_1$	$D^{*0}K^+$	$D^{*+}K^0$	$D_s^*\eta$
$g_1$	1	1	$-\frac{1}{\sqrt{3}}$

The following values are adopted for other parameters [27]:  $\delta = 0.557$ ,  $\beta = 0.4$  GeV,  $f_K = f_\eta = 160$  MeV, and the constituent quark masses  $m_u = m_d = 350$  MeV,  $m_s = 550$  MeV,  $m_c = 1700$  MeV. We note that our numerical results are not sensitive to  $m_c = 1500 \sim 1700$  MeV, while the light quark masses  $m_u = m_d = 330 \sim 350$  MeV and  $m_s = 500 \sim 550$  MeV will lead to about (1 ~ 5)% uncertainties with the final results.

The masses  $M_i$  of the initial states  $1^3P_1$  and  $1^1P_1$   $c\bar{s}$  still have uncertainties. Fortunately, the couplings  $|g_S|$  change only 5% at most when  $M_i \in [2.460, 2.536]$  GeV as shown in Fig. 5. Also it shows that the couplings to  $D^{*0}K^+$  and  $D^{*+}K^0$  are almost the same for each state due to the isospin symmetry. A set of typical  $g_S$  couplings is listed in Table III.

TABLE III: Vertex couplings  $g_S$  at  $M_i = 2.5$  GeV.

$g_S$ (GeV)	$D^{*0}K^+$	$D^{*+}K^0$	$D_s^*\eta$
$1^3P_1$	-7.982	-8.052	2.040
$1^1P_1$	5.644	5.694	-1.443

Apart from the on-shell coupling  $g_S$ , the chiral quark model also provides an exponential momentum-dependent form factor  $\exp(-q_1^2/4\alpha^2)$  as shown in Eqs. (23), (24), (34), and (35). In order to keep this feature in the meson loops, we modify the exponential form factor to a covariant form:

$$\exp\left(-\frac{q_1^2}{4\alpha^2}\right) \rightarrow \exp\left(\frac{q^2 - m^2}{\Lambda^2}\right), \quad (36)$$

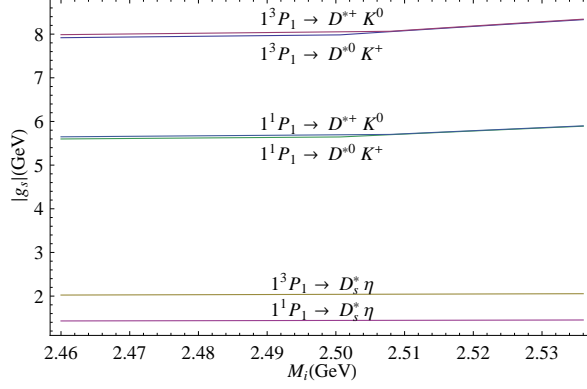


FIG. 5: the absolute values of couplings  $g_s$  as functions of the initial meson mass  $M_i$

where  $q^\mu$  and  $m$  are the four-vector momentum and mass of either  $\mathbb{V}$  or  $\mathbb{P}$  particle. Parameter  $\Lambda$  is the cut-off energy, which can be determined by the quark model, namely, for the  $D^*K$  and  $D_s^*\eta$  loops,

$$\Lambda = 2 \frac{m_c + m_s}{m_c} \left[ \frac{2m_c}{m_c + m_s} \right]^{\frac{1}{4}} \beta = 1.174 \text{ GeV} . \quad (37)$$

The exponential form factor serves to remove the ultraviolet divergence in the loop integrals.

#### IV. THE PROPAGATOR MATRIX

In this Section we will determine the propagator matrix  $G$ . From Eqs. (23) and (24), we have

$$\Pi_a = -\sqrt{2}\Pi_{ab}, \quad \Pi_b = -\Pi_{ab}/\sqrt{2}. \quad (38)$$

So, we only need to calculate the mixing term  $\Pi_{ab}$ . With the AVP coupling form factors, we can explicitly write down  $D_{ab}^{\mu\nu}$  as the following:

$$\begin{aligned} D_{ab}^{\mu\nu} &= \sum g_a g_b \cdot i \int \frac{d^4 k}{(2\pi)^4} \frac{\exp\left(\frac{k^2 - m_v^2}{\Lambda^2}\right) \exp\left(\frac{(k+p)^2 - m_p^2}{\Lambda^2}\right)}{[k^2 - m_v^2][(k+p)^2 - m_p^2]} \left(g^{\mu\nu} - \frac{k^\mu k^\nu}{m_v^2}\right) \\ &\equiv \sum g_a g_b (\Pi g^{\mu\nu} + B' p^\mu p^\nu / p^2) \equiv \sum g_a g_b \text{loop} , \end{aligned} \quad (39)$$

where  $g_a$  and  $g_b$  are the  $S$ -wave couplings of the two vertices, respectively. Comparing with Eq. (8), we obtain

$$\Pi_{ab} \equiv \sum g_a g_b \Pi . \quad (40)$$

The mixing term  $\Pi_{ab}$  can be decomposed into two terms, i.e.

$$\Pi_{ab} \equiv \Pi_{ab}^1 + \Pi_{ab}^2, \quad (41)$$

with

$$\Pi_{ab}^1 \equiv \sum g_a g_b \Pi^1, \quad \Pi_{ab}^2 \equiv \sum g_a g_b \Pi^2, \quad (42)$$

where  $\Pi_{ab}^1$  and  $\Pi_{ab}^2$  are contributions from the  $g^{\mu\nu}$  and  $k^\mu k^\nu$  terms of the vector propagator, respectively.

As follows, we first make an on-shell approximation to investigate the absorptive part. Then, we investigate the full integrals with the help of the exponential form factors.



### A. On-shell approximation

Since the absorptive part of a two-point function is independent of the form factors, the on-shell approximation will allow us to separate out the absorptive part and then compare it with that in a full loop integral. Here we only consider  $\Pi^1$ , for which the loop integral of Eq. (39) in the on-shell approximation becomes

$$loop_1 \xrightarrow{\text{on shell}} g^{\mu\nu} \frac{-i}{16\pi^2} \text{Im} B_0(s, m_p^2, m_v^2) = \Pi^1 g^{\mu\nu} . \quad (43)$$

The resulting mixing term  $\Pi_{ab}$  is a function of  $s$ . We plot  $\Pi_{ab}(\sqrt{s})$  in Fig. 6 with the couplings listed in Table III adopted.

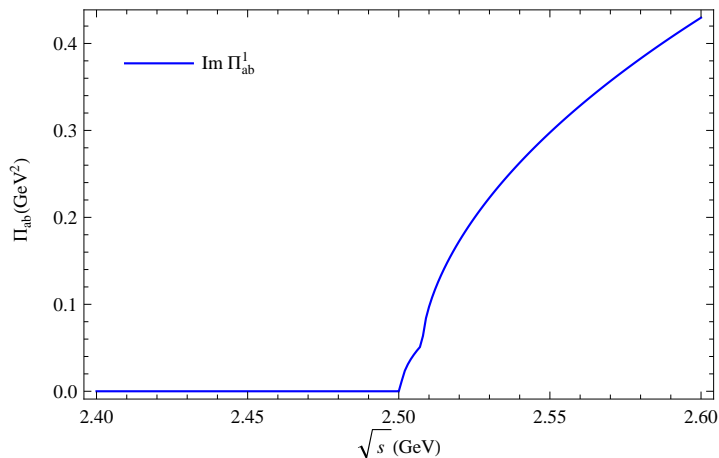


FIG. 6: The mixing term  $\Pi_{ab}$  in the on-shell approximation.

In Fig. 6, two kink structures can be identified. The first one at  $\sqrt{s} = 2.501$  GeV corresponds to the  $D^{*0}K^+$  threshold, and the second one at  $\sqrt{s} = 2.508$  GeV to the  $D^{*+}K^0$  threshold. This result will be compared with the absorptive part in the full loop integrals later.

### B. Full loop calculation with the exponential form factor

In this Subsection we perform the full loop calculation with the exponential form factor. The explicit formula for  $\Pi^1$  is

$$\begin{aligned} loop_1 &= i \int \frac{d^4k}{(2\pi)^4} \frac{\exp\left(\frac{k^2 - m_v^2}{\Lambda^2}\right) \exp\left(\frac{(k+p)^2 - m_p^2}{\Lambda^2}\right)}{[k^2 - m_v^2][(k+p)^2 - m_p^2]} g^{\mu\nu} \\ &= g^{\mu\nu} \frac{-1}{16\pi^2} \int_0^1 dx e^c U(2, 1, \frac{b^2}{a}, a\Delta) = \Pi^1 g^{\mu\nu} \end{aligned} \quad (44)$$

with

$$\begin{aligned} a &\equiv \frac{2}{\Lambda^2} , \\ b^2 &\equiv \frac{(1-2x)^2}{\Lambda^4} s , \\ c &\equiv \frac{s(2x^2 - 2x + 1) - m_p^2 - m_v^2}{\Lambda^2} , \\ \Delta &\equiv (1-x)m_v^2 + xm_p^2 - x(1-x)s . \end{aligned}$$

The explicit formula for  $\Pi^2$  is

$$\begin{aligned}
loop_2 &= (-i) \int \frac{d^4k}{(2\pi)^4} \frac{\exp\left(\frac{k^2 - m_v^2}{\Lambda^2}\right) \exp\left(\frac{(k+p)^2 - m_p^2}{\Lambda^2}\right) k^\mu k^\nu}{[k^2 - m_v^2][(k+p)^2 - m_p^2]} \frac{1}{m_v^2} \\
&= g^{\mu\nu} \frac{1}{32\pi^2 a m_v^2} \int_0^1 dx e^c U\left(2, 0, \frac{b^2}{a}, a\Delta\right) + B_2^U p^\mu p^\nu \\
&\equiv \Pi^2 g^{\mu\nu} + B_2 p^\mu p^\nu,
\end{aligned} \tag{45}$$

where  $a$ ,  $b$ ,  $c$ ,  $\Delta$  are the same as those in Eq. (44). The function  $U(a, b, c, z)$  is a class of special integrals which appears in the evaluation of the loop integrals with exponential form factors. The detailed definition and calculation of  $U(a, b, c, z)$  are provided in Appendix A.

The full loop calculation of the mixing term  $\Pi_{ab}(\sqrt{s})$  is presented in Fig. 7 where the parameters are the same as before. In order to see clearly the contributions from different parts, we also give two sets of the calculated values in Tables IV and V.

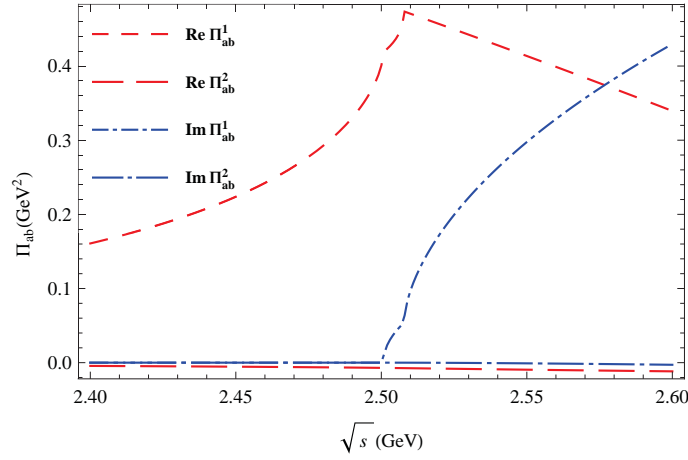


FIG. 7: (color online). The mixing term  $\Pi_{ab}$  with exponential form factors.  $\Pi_{ab}^1$  and  $\Pi_{ab}^2$  are the contributions from the  $g^{\mu\nu}$  term and  $k^\mu k^\nu$  term of the vector propagator, respectively. The dashed lines represent the dispersive parts, while the dot-dashed lines represent the absorptive ones.

TABLE IV: The mixing term  $\Pi_{ab}$  at the pole position  $\sqrt{s} = 2.4545$  GeV.

intermediate state	$D^{*0}K^+$	$D^{*+}K^0$	$D_s^*\eta$	$\Pi_{ab} = \sum g_a g_b \Pi$ (GeV <sup>2</sup> )
$g_a g_b$ (GeV <sup>2</sup> )	-45.05	-53.90	-2.944	—
$\Pi^1$ (on-shell)	0	0	0	0
$\Pi^1$	$-2.391 \times 10^{-3}$	$-2.253 \times 10^{-3}$	$-0.868 \times 10^{-3}$	0.2317
$\Pi^2$	$5.650 \times 10^{-5}$	$5.448 \times 10^{-5}$	$2.503 \times 10^{-5}$	-0.0056

TABLE V: The mixing term  $\Pi_{ab}$  at the pole position  $\sqrt{s} = (2.5449 - 0.0010i)$  GeV.

intermediate state	$D^{*0}K^+$	$D^{*+}K^0$	$D_s^*\eta$	$\Pi_{ab} = \sum g_a g_b \Pi$ (GeV <sup>2</sup> )
$g_a g_b$ (GeV <sup>2</sup> )	-45.05	-53.90	-2.944	—
$\Pi^1$ (on-shell)	$-2.969i \times 10^{-3}$	$-2.718i \times 10^{-3}$	0	0.2803i
$\Pi^1$	$(-4.157 - 2.969i) \times 10^{-3}$	$(-4.260 - 2.718i) \times 10^{-3}$	$-1.389 \times 10^{-3}$	0.4210 + 0.2803i
$\Pi^2$	$(9.419 + 0.886i) \times 10^{-5}$	$(9.059 + 0.678i) \times 10^{-5}$	$3.560 \times 10^{-5}$	-0.0092 - 0.0008i

The loop calculation results help us to learn the following points:

- The imaginary part of  $\Pi_{ab}^1$  with exponential form factors is the same as that in the on-shell approximation. It justifies our calculation method for  $U(a, b, c, z)$  as described in the Appendix.
- The contribution from the term of  $g^{\mu\nu}$  is dominant. The open thresholds of  $D^{*0}K^+$  and  $D^{*+}K^0$  cause two kinks in both real and imaginary parts. With the increase of  $\sqrt{s}$ ,  $\text{Re}\Pi_{ab}^1$  first increases until it reaches a summit at the  $D^{*+}K^0$  threshold. It then decreases in a linear behavior in terms of  $\sqrt{s}$ . In contrast,  $\text{Im}\Pi_{ab}^1$  is zero below the  $D^{*0}K^+$  threshold and then increases quickly when the decay thresholds are open. One can see that below the  $D^{*0}K^+$  threshold, the real part is the only contribution and cannot be neglected. The imaginary part becomes significant above 2.53 GeV.
- The calculation also shows that the contributions from the  $k^\mu k^\nu$  term of the vector propagator are negligible. Near the threshold, the momentum is small such that  $\Pi_{ab}^2$  suffers an  $O(1/m_v^2)$  suppression comparing to  $\Pi_{ab}^1$  in both the absorptive and dispersive part.
- The contributions from the  $D^*K$  loops are found dominant, while the contributions from  $D_s^*\eta$  account for only about 1% of the mixing term due to the rather small coupling value in the  $D_s^*\eta$  loop.

## V. POLE POSITIONS AND MIXING PARAMETERS

With the  $\Pi_{ab}(s)$  determined, we can directly search for poles for the physical states in the propagator matrix  $G$  in Eq. (10). We adopt the following bare  $c\bar{s}$  masses,  $m[{}^3P_1] = 2.57$  GeV and  $m[{}^1P_1] = 2.53$  GeV, from the Godfrey-Isgur (GI) model [15] as input. By scanning over the energy  $\sqrt{s}$ , the requirement of  $|\det[\bar{G}(s)]| = 0$  provides a direct access to the pole positions as shown in Fig. 8. Two possible poles near 2.46 GeV and 2.54 GeV are highlighted. When varying the cut-off parameter  $\Lambda$  in Eq. (37) within the range of  $[1.174 - 0.22, 1.174 + 0.22]$  GeV, it shows that the higher pole is stable and the lower one changes from 2.47 GeV to 2.44 GeV. Searching for the poles on the complex energy plane, we can pin down the masses and widths of these two poles as listed in Table VI. It shows that the mass of  $D_{s1}(2460)$  changes 3.6 MeV at most with or without the contribution from the  $k^\mu k^\nu$  term of the propagator, while the mass of  $D_{s1}(2536)$  changes only 0.1 MeV. The extracted mass of  $D_{s1}(2460)$  is only 5 MeV below the experiment value, and the mass of  $D_{s1}(2536)$  is only 10 MeV above the experiment one. In principle, the Okubo-Zweig-Iizuka (OZI) rule allowed hadronic decay width of  $D_{s1}(2460)$  is zero. The obtained width 2.0 MeV for  $D_{s1}(2536)$  seems to be slightly larger than the experiment value 0.92 MeV, but can still be regarded as in good agreement. In brief, our prediction for the masses and widths of these two states agrees well with the experiment data.

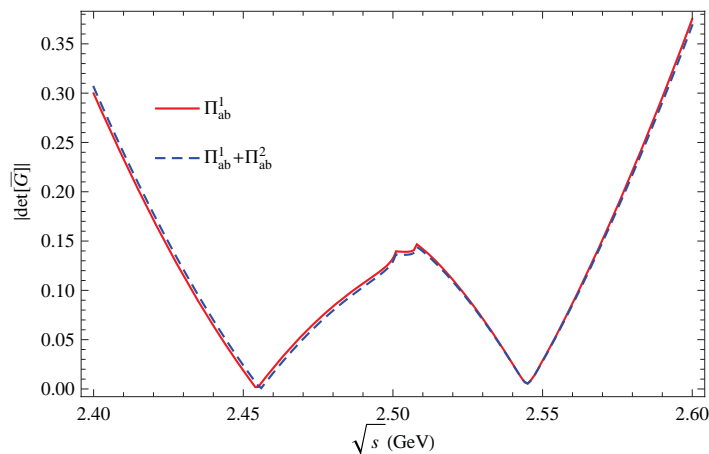


FIG. 8: Pole structures highlighted by the zero values of  $\det[\bar{G}]$  in the propagator matrix.

Before extracting the mixing parameters, we show that our formalisms can reproduce the ideal mixing angle  $\theta_0$  in the heavy quark limit. In this limit,  $m_a$  and  $m_b$  are degenerate. From Eqs. (11) and (38), we only need to diagonalize the simple matrix

$$\begin{pmatrix} -\frac{1}{\sqrt{2}} & -1 \\ -1 & -\sqrt{2} \end{pmatrix}, \quad (46)$$

TABLE VI: Masses and widths obtained from the pole analysis.

$[m - i\frac{\Gamma}{2}]$ (MeV)	$D_{s1}(2460)$	$D_{s1}(2536)$
$\Pi_{ab}^1$	2454.5	2544.9 - 1.0 <i>i</i>
$\Pi_{ab}^1 + \Pi_{ab}^2$	2455.8	2544.9 - 1.1 <i>i</i>
Experiment	2459.5	2535.08 - 0.46 <i>i</i>

which immediately leads to  $\theta_0 = \arctan[1/\sqrt{2}] = 35.26^\circ$ .

Now we proceed to the extraction of the mixing parameters  $\{\theta, \phi\}$  by diagonalizing  $\bar{G}(s)$  with  $\sqrt{s}$  fixed at the poles. When  $\bar{G}$  is a complex matrix, we try to approach the diagonal limit  $R\bar{G}_{ab}R^\dagger = \bar{G}_{AB}$  in three ways: Method I, set  $\bar{G}_{12}^{AB} = 0$ ; Method II, set  $\bar{G}_{21}^{AB} = 0$ ; and Method III, minimize  $|\bar{G}_{12}^{AB}| + |\bar{G}_{21}^{AB}|$ . The results from these three diagonalization schemes are listed in Table VII. As we expected before, the mixing angles of these two states determined at their pole masses are indeed different. For  $D_{s1}(2460)$ ,  $\bar{G}$  is a symmetric real matrix. So the mixing parameters are the same in these three methods:  $\theta = 47.6^\circ$ ,  $\phi = 0^\circ$ . From the mixing scheme in Eq. (4),  $\theta > 45^\circ$  means that the  $^1P_1$  component is larger than the  $^3P_1$  in  $D_{s1}(2460)$ . This mixing pattern would affect the mass shift as we will show later. The result corresponds to  $\theta' = 12.3^\circ$  in the  $j = 1/2$  and  $j = 3/2$  mixing in the heavy quark limit. For  $D_{s1}(2536)$ ,  $\bar{G}$  is a complex matrix. The mixing angle  $\theta = 39.7^\circ$  determined at the  $D_{s1}(2536)$  mass changes little in those three methods, while the relative phase suffers an uncertainty of  $\phi = -6.9^\circ \sim 6.9^\circ$ . We will show later in Sec. VI that the mixing angle  $\theta = 39.7^\circ$  is consistent with the experimental constraints and can be useful for picking up one of those two solutions from the experimental fit. Again from the mixing scheme,  $\theta < 45^\circ$  means that the  $^1P_1$  component is larger than the  $^3P_1$  one in  $D_{s1}(2536)$ . The result corresponds to  $\theta' = 4.4^\circ$  in the  $j = 1/2$  and  $j = 3/2$  mixing bases. The energy dependence of the mixing angle reflects the breaking of orthogonality among these two physical states.

TABLE VII: The mixing angle  $\theta$  and relative phase  $\phi$  extracted at the two poles in those three diagonalization schemes.

$\{\theta, \phi\} [^\circ]$	$D_{s1}(2460)$			$D_{s1}(2536)$		
	I	II	III	I	II	III
$\Pi_{ab}^1$	{47.5, 0}	{47.5, 0}	{47.5, 0}	{39.7, -6.4}	{39.7, 6.4}	{39.7, 0}
$\Pi_{ab}^1 + \Pi_{ab}^2$	{47.6, 0}	{47.6, 0}	{47.6, 0}	{39.8, -6.5}	{39.8, 6.5}	{39.7, 0}

From the mixing angle analysis, we also learn that the  $D_{s1}(2460)$  has a larger  $j = 1/2$  component which couples to the  $D^*K$  through an  $S$ -wave. It hence acquires a significant mass shift  $\sim 100$  MeV through meson loop corrections. In contrast, the  $D_{s1}(2536)$  contains a larger  $j = 3/2$  component which couples to the  $D^*K$  through a  $D$ -wave. It only gains a small mass shift  $\sim 10$  MeV.

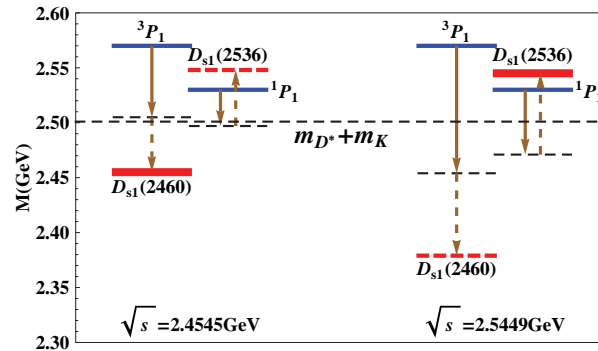


FIG. 9: (color online). Schematic plot for the mass-shift procedure. The thin solid bars represent the original  $^3P_1$  and  $^1P_1$  states in the quark model. The thick solid bars represent the two physical states  $D_{s1}(2460)$  (left) and  $D_{s1}(2536)$  (right). The solid arrows represent the mass shifts due to the diagonal elements  $\Pi_a$  and  $\Pi_b$ , while the dashed arrows represent those due to the off-diagonal element  $\Pi_{ab}$ . The threshold for  $D^*K$  is shown by the horizontal dashed line.

The mass shift procedure is also an interesting issue and can help us to understand why  $D_{s1}(2460)$  has a larger  $^1P_1$  component. As shown in Fig. 9 and Table VIII, we can decompose the mass shift procedure into two classes,

TABLE VIII: Mass shift procedure at different  $\sqrt{s}$ . From  $\sqrt{M_{ab}^2}$ , we can see the mass shifts due to  $\Pi_a$  and  $\Pi_b$ , while from  $\sqrt{M_{AB}^2}$ , further mass shifts due to  $\Pi_{ab}$  can be learned. Here we only present the results from the quasi-diagonalization method II.

$\sqrt{s}$ GeV	bare mass (GeV)	$\sqrt{M_{ab}^2}$ (GeV)	$\sqrt{M_{AB}^2}$ (GeV)
2.4545 GeV	$\begin{bmatrix} 2.53 & 0 \\ 0 & 2.57 \end{bmatrix}$	$\begin{bmatrix} 2.497 & 0.481i \\ 0.481i & 2.505 \end{bmatrix}$	$\begin{bmatrix} 2.548 & 0 \\ 0 & 2.455 \end{bmatrix}$
2.5449 GeV		$\begin{bmatrix} 2.471 - 0.040i & 0.206 - 0.678i \\ 0.206 - 0.678i & 2.454 - 0.080i \end{bmatrix}$	$\begin{bmatrix} 2.545 - 0.001i & 0.141 + 0.303i \\ 0 & 2.379 - 0.123i \end{bmatrix}$

i.e. diagonal shift and off-diagonal shift. The diagonal elements  $\Pi_a$  and  $\Pi_b$  cause both  $^3P_1$  and  $^1P_1$  states to move downwards, while the off-diagonal elements  $\Pi_{ab}$  make one state to shift up and the other to shift down. At  $\sqrt{s} = 2.46$  GeV, after the diagonal shift the  $^3P_1$  state is still higher than the  $^1P_1$ . But after the off-diagonal shift, the higher mass state moves down to become an on-shell  $D_{s1}(2460)$  and the lower state moves up to become a virtual  $D_{s1}(2536)$ . The reversal of the mass ordering results in a mixing angle  $\theta > 45^\circ$  and thus a larger  $^1P_1$  component in  $D_{s1}(2460)$ . At  $\sqrt{s} = 2.54$  GeV, after the diagonal shift the  $^1P_1$  becomes higher than the  $^3P_1$ . Then after the off-diagonal shift, the higher state becomes much higher and the lower much lower, which causes a mixing angle  $\theta < 45^\circ$  and a larger  $^1P_1$  component in  $D_{s1}(2536)$ . Note that in this situation the on-shell state corresponds to the  $D_{s1}(2536)$ , and the  $D_{s1}(2460)$  appear as a virtual one.

## VI. EXPERIMENTAL CONSTRAINTS ON THE MIXING ANGLE

In this part, we come to survey the constraints for the mixing angle  $\theta$  from experiments. The strong decays of  $D_{s1}(2536)$  has been measured with reasonable precision which are summarized in Table IX. Since the  $D^*K$  channel is the only allowed strong decay channel for  $D_{s1}(2536)$ , it is a good approximation to assume

$$\Gamma[D_{s1}(2536)] \approx \Gamma(D_{s1}(2536) \rightarrow D^*K), \quad (47)$$

which can be estimated in the chiral quark model. The partial width fractions  $R_1$  and  $R_2$  can also be calculated and compared with the data.

TABLE IX: The available experimental status of  $D_{s1}(2536)$ .

$m = 2535.08 \pm 0.01 \pm 0.15$ MeV, $\Gamma = 0.92 \pm 0.03 \pm 0.04$ MeV (BaBar [30])
$R_1 = \frac{\Gamma(D^*(2007)^0 K^+)}{\Gamma(D^*(2010)^+ K^0)} = 1.36 \pm 0.20$ (PDG2010 [1])
$R_2 = \frac{\Gamma(D^*(2010)^+ K^0)_{S\text{-wave}}}{\Gamma(D^*(2010)^+ K^0)} = 0.72 \pm 0.05 \pm 0.01$ (Belle [31])

The helicity amplitudes for  $1^3P_1 \rightarrow D^*K$  and  $1^1P_1 \rightarrow D^*K$  have been listed in Eqs. (20) and (21). The partial width can be obtained by [27]

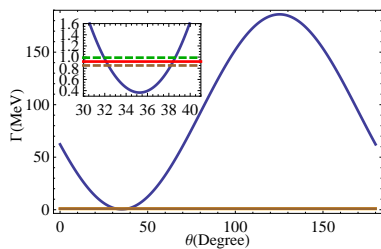
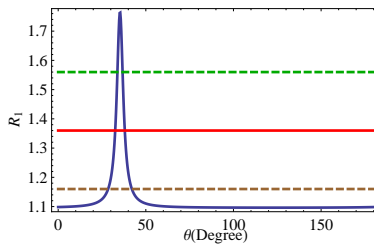
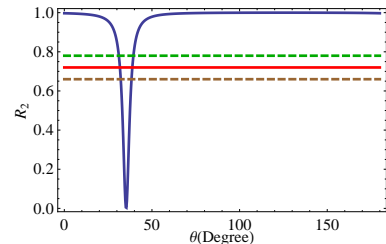
$$\Gamma = \left( \frac{\delta}{f_m} \right)^2 \frac{(E_f + M_f)|\vec{q}|}{4\pi M_i(2J_i + 1)} \sum_\nu |A_\nu^q|^2, \quad (48)$$

where  $J_i$  is the spin of the initial particle. In order to calculate  $R_2$ , we need to extract the  $S$ -wave components from the helicity amplitudes. By defining  $A_S = \frac{G_S}{2\sqrt{\pi}}$  and  $A_D = \frac{G_D}{2\sqrt{\pi}}$ , we deduce from Eq. (15)

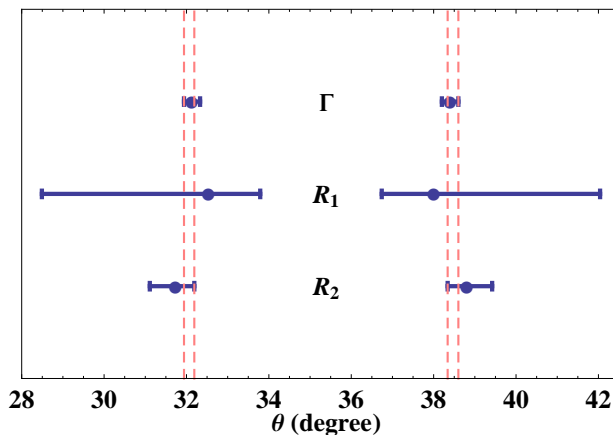
$$\begin{cases} A_0 = A_S - \sqrt{2}A_D \\ A_1 = A_S + \frac{1}{\sqrt{2}}A_D \end{cases} \Rightarrow \begin{cases} A_S = \frac{1}{3}(A_0 + 2A_1) \\ A_D = -\frac{\sqrt{2}}{3}(A_0 - A_1) \end{cases}, \quad (49)$$

where the  $S$  and  $D$ -wave components have been separated out. We use the same model parameters as before to calculate the partial width  $\Gamma[D_{s1}(2536)]$  and ratios  $R_1$  and  $R_2$  in terms of the mixing angle  $\theta$ . The results are shown in Figs. (10)-(13).

A similar result as Fig. 10 for  $\Gamma[D_{s1}(2536)]$  in terms of  $\theta$  has been given in Ref. [27] but with the notation  $\theta \rightarrow \phi + 90^\circ$ . Those three horizontal lines in Figs. (10)-(12) represent the upper limits, center values, and lower

FIG. 10:  $\Gamma[D_{s1}(2536)]$  as a function of  $\theta$ FIG. 11:  $R_1$  as a function of  $\theta$ FIG. 12:  $R_2$  as a function of  $\theta$ 

limits of the experimental data. The interesting feature arising from the results of Figs. (10)-(12) is that the overlaps between the experimental data and theoretical values are separated into two narrow bands of  $\theta$  which are located symmetric to the ideal mixing angle  $\theta_0 = 35.26^\circ$ , i.e.  $\theta_1 \simeq 32.1^\circ$  or  $\theta_2 \simeq 38.4^\circ$ . An alternative way to present the results is via Fig. 13, where the overlapped  $\theta$  values are denoted by the vertical dashed lines, while the experimental observables with errors are presented in terms of  $\theta$ . Notice that these two bands of  $\theta$  are both smaller than  $45^\circ$ . Therefore, based on the present experimental measurements, one cannot determine which value for  $\theta$  should be taken. It turns out that our analysis in Sec. V can precisely pick up one of these two solutions, namely,  $\theta_2 \simeq 38.4^\circ$  is favored in comparison with the theoretical value  $\theta = 39.7^\circ$ .

FIG. 13: The experimental constraints on the mixing angle  $\theta$ .

## VII. SUMMARY

In summary, we have studied the mixing mechanism for the axial vector states  $D_{s1}(2460)$  and  $D_{s1}(2536)$  via the  $S$ -wave intermediate meson loops. We establish the propagator matrix for this two-state system. Then, by searching for the pole structures in the propagator matrix, we can pin down the masses and widths of the physical states. The mixing angle and relative phase between the  $^3P_1$  and  $^1P_1$  components can be determined by diagonalizing the propagator matrix. For  $D_{s1}(2460)$ , we obtain  $m = 2454.5$  MeV,  $\theta = 47.5^\circ$  and  $\phi = 0^\circ$ . For  $D_{s1}(2536)$ , we find  $m = 2544.9 - 1.0i$  MeV,  $\theta = 39.7^\circ$ , and  $\phi = -6.9^\circ \sim 6.9^\circ$ . Our results agree well with the experimental measurement. In particular, the new BaBar measurement put a strong constraint on the mixing angle at the mass of  $D_{s1}(2536)$  with two solutions,  $\theta_1 \simeq 32.1^\circ$  and  $\theta_2 \simeq 38.4^\circ$ . Our theoretical calculation finds  $\theta = 39.7^\circ$  which is in good agreement with  $\theta_2$ .

Note that due to the breaking of orthogonality the energy-dependent mixing angles defined at the different physical masses turn out to have different values. We find that both  $D_{s1}(2460)$  and  $D_{s1}(2536)$  have a relatively large  $^1P_1$  component in their wavefunctions.

It is also interesting to learn the important role played by the coupled channel effects for states near open thresholds. For states that can couple to each other via the coupled channels, the two-state propagator matrix carries rich

information about the mixing and mass shifts as a manifestation of the underlying dynamics. Extension of such a study to other axial-vector meson mixings would be useful for deepen our understanding of the coupled channel effects and their impact on the hadron spectrum.

### Acknowledgments

This work is supported, in part, by National Natural Science Foundation of China (Grant No. 11035006), Chinese Academy of Sciences (KJCX2-EW-N01), and Ministry of Science and Technology of China (2009CB825200).

### Appendix A: Calculation of function $U(a, b, c, z)$

Initially we define

$$U(a, b, c, z) = \frac{1}{\Gamma(a)} \int_0^\infty dt t^{a-1} (1+t)^{b-a-1} \exp\left(-zt - \frac{c}{1+t}\right), \quad (\text{A1})$$

which is the typical integral we encounter in the calculation. A special case,  $U(a, b, c=0, z) = U(a, b, z)$ , is the Tricomi confluent hypergeometric function, which is a build-in function in Mathematica. The function  $U(a, b, z)$  is a single-valued function on the  $z$ -plane cut along the interval  $(-\infty, 0]$ , where it is continuous from above, i.e.

$$\text{when } z < 0, \quad U(a, b, z) = \lim_{\epsilon \rightarrow 0^+} U(a, b, z + i\epsilon). \quad (\text{A2})$$

Function  $U(a, b, c, z)$  as a physical quantity should be analytic with respect to its arguments. However, the integral in Eq. (A1) only converges when  $Re(z) > 0$  and  $Re(a) > 0$ . In order to analytically continue the integral to  $Re(z) < 0$ , we make a change in variables  $zt = x (z > 0)$ . Hence, Eq. (A1) becomes

$$U(a, b, c, z) = \frac{z^{1-b}}{\Gamma(a)} \int_0^\infty dx x^{a-1} (x+z)^{b-a-1} \exp\left(-x - \frac{cz}{x+z}\right). \quad (\text{A3})$$

In the region  $Re(z) > 0$ , Eq. (A1) and (A3) are exactly equivalent to each other when  $Re(b) < 2$ . The difference between them can be expressed by the integral over  $C_R$  in Fig. 14(a).

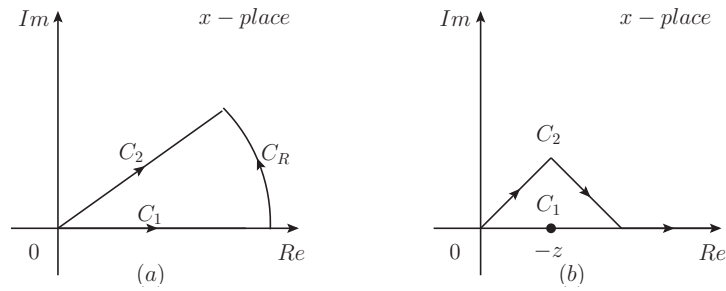


FIG. 14: The continuation of  $U(a, b, c, z)$

When  $Re(b) < 2$ , the contribution from  $C_R$  is zero. Comparing with Eq. (A1), the integral in Eq. (A3) has larger convergent region, i.e. the whole complex  $z$ -plane except  $z < 0$ . When  $z < 0$ , there is a singular point at  $x = -z$  in the integral path as shown in Fig. 14(b). Considering Eq. (A2),  $U(a, b, c, z)$  must satisfy a similar requirement. It means that the integral path  $C_1$  in Fig. 14(b) should be replaced by the integral path  $C_2$ . Using the expression in Eq. (A3) and the replacement in Fig. 14(b), we can analytically continue the integral in Eq. (A1) to the whole  $z$ -plane. The constraints of the above method are  $Re(a) > 0$  and  $Re(b) < 2$ , which could satisfy our present need.

To test this method, we compare the results for  $U(a, b, z)$  in Fig. 15 using our method and the build-in Mathematica program. It shows that these two calculations are in good agreement to each other. This test is done at  $c = 0$ . Since  $c$  in Eq. (A3) does not bring either new divergence problems or new singular points, we can justify that our analytic continuation of  $U(a, b, c, z)$  is quite reliable and generally applicable.

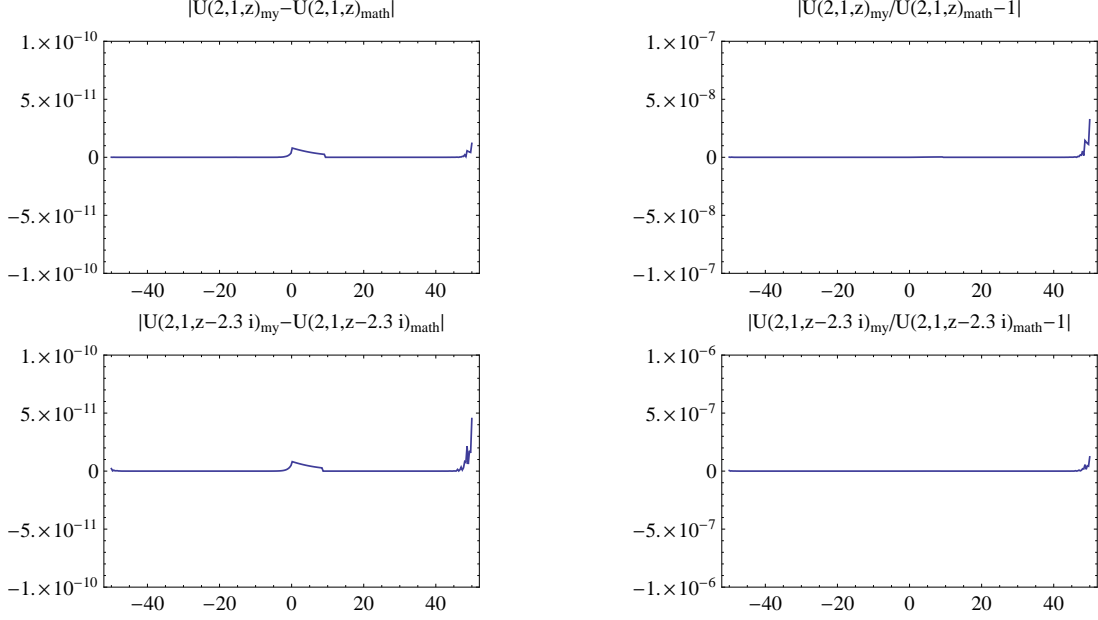


FIG. 15: Test the accuracy and precision of the analytic continuation of  $U(a, b, c, z)$ .

- 
- [1] K. Nakamura et al. (Particle Data Group), J. Phys. **G37**, 075021 (2010).
  - [2] B. Aubert et al. (BABAR Collaboration), Phys.Rev.Lett. **90**, 242001 (2003), hep-ex/0304021.
  - [3] P. Krokovny et al. (Belle Collaboration), Phys.Rev.Lett. **91**, 262002 (2003), hep-ex/0308019.
  - [4] D. Besson et al. (CLEO Collaboration), Phys.Rev. **D68**, 032002 (2003), hep-ex/0305100.
  - [5] E. S. Swanson, Phys.Rept. **429**, 243 (2006), hep-ph/0601110.
  - [6] S. Godfrey, Phys.Rev. **D72**, 054029 (2005), hep-ph/0508078.
  - [7] Y. Simonov and J. Tjon, Phys.Rev. **D70**, 114013 (2004), hep-ph/0409361.
  - [8] A. M. Badalian, Y. A. Simonov, and M. A. Trusov, Phys. Rev. **D77**, 074017 (2008), 0712.3943.
  - [9] S. Coito, G. Rupp, and E. van Beveren (2011), 1106.2760.
  - [10] J.-J. Wu, Q. Zhao, and B. S. Zou, Phys. Rev. **D75**, 114012 (2007), 0704.3652.
  - [11] F. Close and E. Swanson, Phys.Rev. **D72**, 094004 (2005), hep-ph/0505206.
  - [12] T. Barnes, F. Close, and H. Lipkin, Phys.Rev. **D68**, 054006 (2003), hep-ph/0305025.
  - [13] A. Faessler, T. Gutsche, V. E. Lyubovitskij, and Y.-L. Ma, Phys.Rev. **D76**, 114008 (2007), 0709.3946.
  - [14] F.-K. Guo, P.-N. Shen, and H.-C. Chiang, Phys.Lett. **B647**, 133 (2007), hep-ph/0610008.
  - [15] S. Godfrey and N. Isgur, Phys. Rev. **D32**, 189 (1985).
  - [16] Y. Yamada, A. Suzuki, M. Kazuyama, and M. Kimura, Phys.Rev. **C72**, 065202 (2005), hep-ph/0601211.
  - [17] Z.-Y. Zhou and Z. Xiao, Phys.Rev. **D84**, 034023 (2011), 1105.6025.
  - [18] B. S. Zou and F. Hussain, Phys. Rev. **C67**, 015204 (2003), hep-ph/0210164.
  - [19] A. Manohar and H. Georgi, Nucl.Phys. **B234**, 189 (1984).
  - [20] Z.-p. Li, H.-x. Ye, and M.-h. Lu, Phys.Rev. **C56**, 1099 (1997), nucl-th/9706010.
  - [21] Q. Zhao, Z.-p. Li, and C. Bennhold, Phys.Lett. **B436**, 42 (1998), nucl-th/9803015.
  - [22] Q. Zhao, Z.-p. Li, and C. Bennhold, Phys. Rev. **C58**, 2393 (1998), nucl-th/9806100.
  - [23] Q. Zhao, J. Al-Khalili, Z. Li, and R. Workman, Phys.Rev. **C65**, 065204 (2002), nucl-th/0202067.
  - [24] Q. Zhao, B. Saghai, and Z.-p. Li, J.Phys.G **G28**, 1293 (2002), nucl-th/0011069.
  - [25] X.-H. Zhong, Q. Zhao, J. He, and B. Saghai, Phys.Rev. **C76**, 065205 (2007), 0706.3543.
  - [26] X.-H. Zhong and Q. Zhao, Phys.Rev. **C84**, 045207 (2011), 1106.2892.
  - [27] X.-h. Zhong and Q. Zhao, Phys. Rev. **D78**, 014029 (2008), 0803.2102.
  - [28] X.-H. Zhong and Q. Zhao, Phys.Rev. **D81**, 014031 (2010), 0911.1856.
  - [29] D. O. Riska and G. E. Brown, Nucl. Phys. **A679**, 577 (2001), nucl-th/0005049.



- [30] J. Lees et al. (The BABAR Collaboration), Phys.Rev. **D83**, 072003 (2011), 1103.2675.
- [31] V. Balagura et al. (Belle), Phys. Rev. **D77**, 032001 (2008), 0709.4184.